Article

Neuron

During Running in Place, Grid Cells Integrate Elapsed Time and Distance Run

Highlights

- Time and distance coding by grid cells can be studied in rats running in place
- In this task, grid cell activity reflects a combination of time and distance coding
- Grid cells are more sharply tuned to time and distance than non-grid cells
- Many grid cells exhibit multiple time and distance fields

Authors

Benjamin J. Kraus, Mark P. Brandon, Robert J. Robinson, Michael A. Connerney, Michael E. Hasselmo, Howard Eichenbaum

Correspondence

bkraus@bu.edu (B.J.K.), hbe@bu.edu (H.E.)

In Brief

Grid cells encode a periodic array of locations occupied as rats move through space. Kraus et al. show that, when cues about motion through locations are eliminated, grid cells integrate self-generated distance and time information that predominate in that experience.

Kraus et al., 2015, Neuron *88*, 578–589
November 4, 2015
http://dx.doi.org/10.1016/j.neuron.2015.09.031

CellPress

CellPress

Neuron
Article

During Running in Place, Grid Cells Integrate Elapsed Time and Distance Run

Benjamin J. Kraus,[1,*] Mark P. Brandon,[2] Robert J. Robinson II,[1] Michael A. Connerney,[1] Michael E. Hasselmo,[1] and Howard Eichenbaum[1,*]
[1]Center for Memory and Brain, Boston University, Boston, MA 02215, USA
[2]Department of Psychiatry, Douglas Mental Health University Institute, McGill University, Montreal, QC H4H 1R3, Canada
*Correspondence: bkraus@bu.edu (B.J.K.), hbe@bu.edu (H.E.)
http://dx.doi.org/10.1016/j.neuron.2015.09.031

SUMMARY

The spatial scale of grid cells may be provided by self-generated motion information or by external sensory information from environmental cues. To determine whether grid cell activity reflects distance traveled or elapsed time independent of external information, we recorded grid cells as animals ran in place on a treadmill. Grid cell activity was only weakly influenced by location, but most grid cells and other neurons recorded from the same electrodes strongly signaled a combination of distance and time, with some signaling only distance or time. Grid cells were more sharply tuned to time and distance than non-grid cells. Many grid cells exhibited multiple firing fields during treadmill running, parallel to the periodic firing fields observed in open fields, suggesting a common mode of information processing. These observations indicate that, in the absence of external dynamic cues, grid cells integrate self-generated distance and time information to encode a representation of experience.

INTRODUCTION

Grid cells are neurons that fire when a rodent occupies any of a periodic array of locations within an open field (Hafting et al., 2005). Based on the observations that grid cell firing patterns persist when external visual information is removed and the same periodic spatial pattern is maintained across environments, it has been suggested that grid cells might update the animal's location by integrating path-based self-generated motion cues (McNaughton et al., 2006; Moser et al., 2008). In addition, path integration can be accomplished based on time traveled at a constant speed (Huth, 2013), and there is considerable evidence that temporal signals are generated in a network of cortical and striatal areas that contribute to timing and provide direct or indirect inputs to the medial entorhinal cortex (MEC) (Davis et al., 2009; Janssen and Shadlen, 2005; Kim et al., 2013; Matell et al., 2003a, 2003b; Roberts et al., 2013; Watrous et al., 2013). Also, grid cells depend on inputs from the hippocampus (Bonnevie et al., 2013), which is known to represent temporal information (Kraus et al., 2013; MacDonald et al., 2011, 2013; Naya and Suzuki, 2011; Pastalkova et al., 2008). However, there is no direct evidence that grid cells represent either distance traveled or time elapsed during movement. In addition, there is strong evidence that external visual inputs also strongly influence the firing patterns of grid cells: grid cell firing patterns are anchored to external landmarks (Barry et al., 2007; Hafting et al., 2005), have access to current heading direction (Sargolini et al., 2006; Taube, 1995), and are influenced by experience in an environment (Barry et al., 2012), its structure (Derdikman et al., 2009), and geometry (Barry et al., 2007; Krupic et al., 2015; Stensola et al., 2012). These findings have led Poucet et al. (2014) to challenge the idea that grid cells provide a distance metric based on self-generated cues alone, although they allow that grid cells might signal distance when visual cues are absent. Here, we explored the extent to which grid cells are activated based on location, time, and distance cues by recording their activity as rats ran in place on a treadmill in a visually rich environment. We report that grid cells provide an integrated representation of self-generated distance and time information in a situation where visual-spatial cues are present but visual flow is eliminated.

Rats performed a spatial alternation task on a figure-eight maze (Figure 1A; Movie S1) in which, on each trial, they ran for 14–20 s at 30–49 cm/s on a motorized treadmill embedded in the center stem of the maze. On individual sessions, either the duration (16 s) or the distance of the run (700 cm) was fixed, and the treadmill speed varied randomly across trials. In four rats over 136 recording sessions, 177 cells were classified as grid cells based on spatial firing patterns during open field foraging (see Experimental Procedures). Their firing properties were compared with 147 non-grid cells recorded simultaneously on the same tetrodes (Tables S1 and S2). Although cells were recorded from the MEC and neighboring areas (Experimental Procedures; Figures S2 and S3), grid cells from all regions were similar in their gridness and other features of spatial coding (Figures S5E–S5G), and so these populations were combined to explore whether grid cells defined by their spatial coding properties also encode time or distance.

RESULTS

Grid Cell Firing Patterns Are Modulated by Time and Distance as Rats Run in Place

Our initial analyses focused on whether grid and non-grid cells fired continuously during running in fixed place—as might be

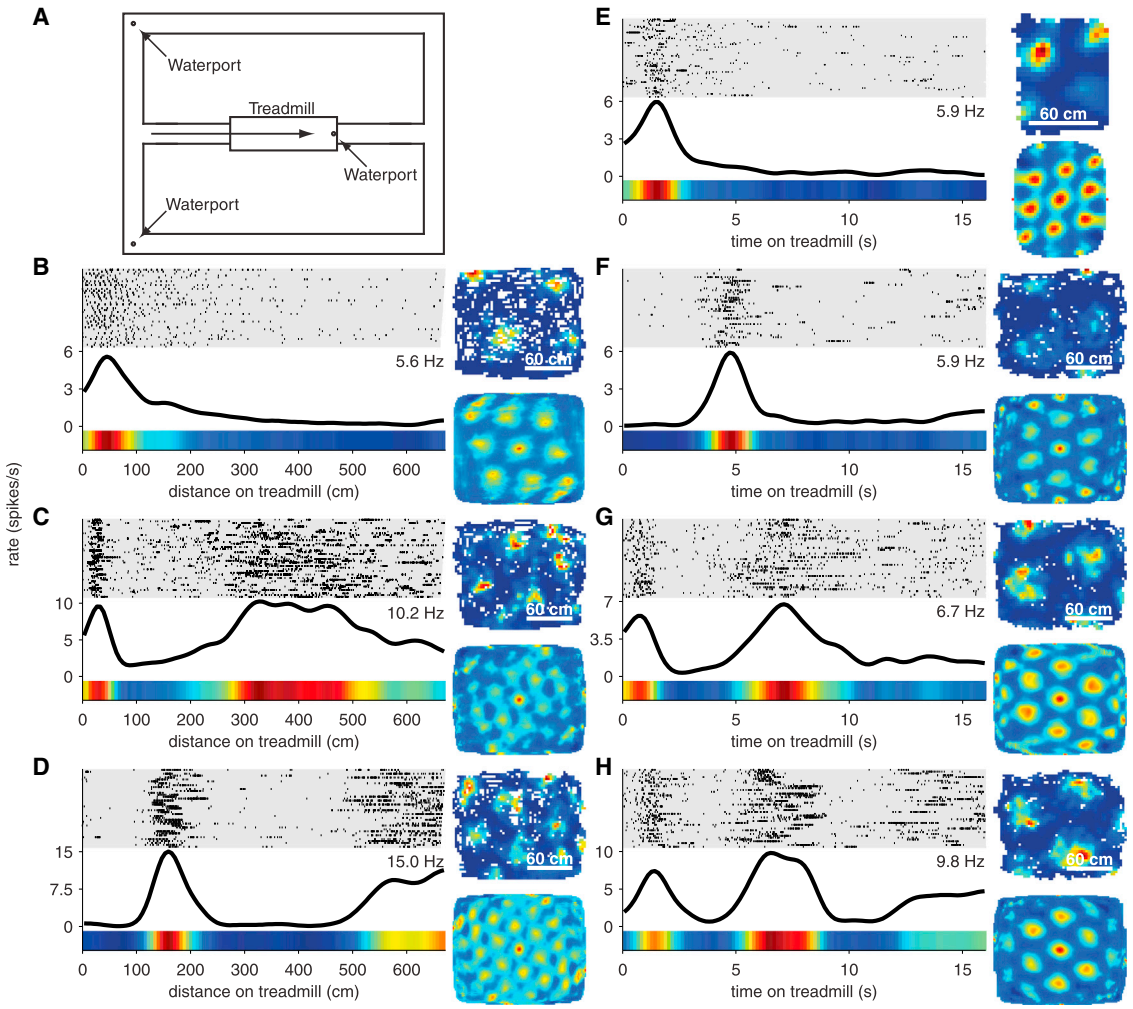

Figure 1. Grid Cells Fire at Specific Times and Distances during Treadmill Running

(A) Maze with treadmill in the center stem.

(B–H) In (B–F), example grid cells show their firing patterns during treadmill running in raster plots (left-top), histograms of average firing over time (left-middle), and normalized firing rate plots (left-bottom) and their open field spatial firing patterns (right-top) and spatial autocorrelations (right-bottom). In distance-fixed sessions (B–D), activity is plotted in terms of distance run during treadmill runs; in time-fixed sessions (E–H), activity is plotted in terms of elapsed time. The activity during treadmill running of the grid cell in (D) is shown in Movie S1. Figure S1 includes additional examples, including firing activity during maze traversal (when the treadmill is stopped).

See also Figure S1 and Movie S1.

expected if they represent allocentric location (Hartley et al., 2014)—or varied in firing rate, indicating influences of self-generated information about elapsed time or distance run. We found many grid cells that fired at specific distances run (most easily observed in distance-fixed sessions, e.g., Figures 1B–1D; Figures S1A–S1C) or at specific moments (most easily observed in time-fixed sessions, e.g., Figures 1E–1H and S1D–S1F). Indeed, most grid cells (162; 92%), as well as most non-grid cells (113; 77%), fired at specific moments or distances during treadmill running. Similar to previous observations of CA1 neurons in animals performing the same task (Kraus et al., 2013), many of these same neurons also expressed firing fields in other regions of the maze when the treadmill was off (Figure S1).

To evaluate the distributions of grid and non-grid cells that encode time or distance, we initially combined the data from time-fixed and distance-fixed sessions using a measure of the fraction of the total run (in time or distance; see Experimental Procedures). We found that the firing fields of both grid and non-grid cells were distributed across the entire treadmill run (Figures 2A and 2B; Figures S2A–S2D). Overall, grid cells more precisely measured run position than other types of neurons recorded in the same brain areas. Thus, grid cells had significantly narrower firing fields than non-grid cells (Kolmogorov-Smirnov test: $p = 2 \times 10^{-10}$; Wilcoxon rank-sum test: $p = 1 \times 10^{-7}$; Figures 2D and S2E) and were characterized by significantly sharper tuning (peak firing rate divided by average firing rate) compared to non-grid cells (Kolmogorov-Smirnov test: $p = 7 \times 10^{-15}$;

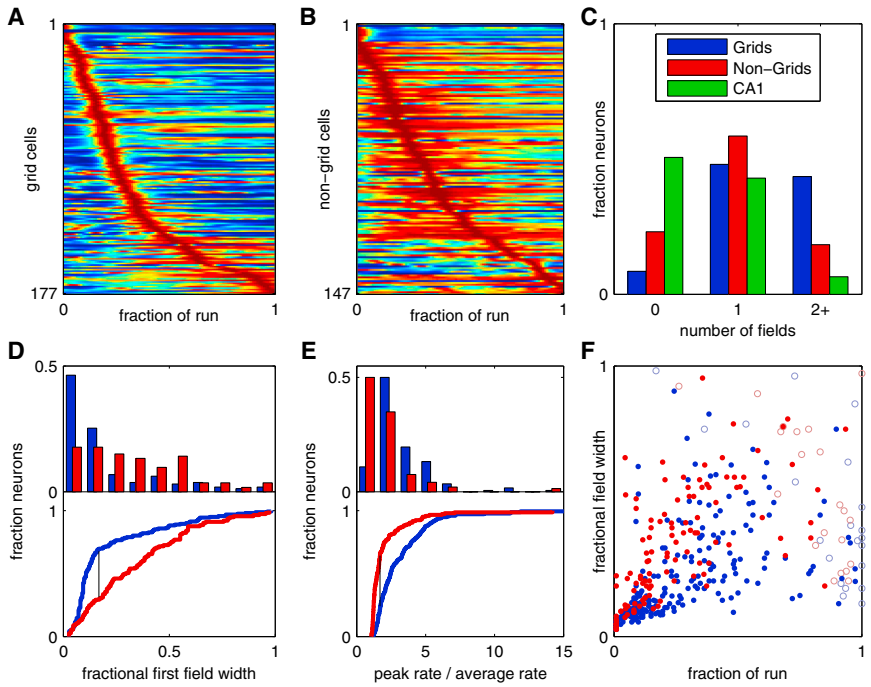

Figure 2. Characteristics of Grid Cells during Treadmill Running

(A and B) Ensemble firing rate maps showing normalized spiking rate during treadmill running for grid cells (A) and non-grid cells (B). Firing rate is plotted in terms of "fraction of run" to allow ensemble analysis across both time-fixed and distance-fixed sessions.

(C–F) In (C), distribution is shown of the number of firing fields observed for each type of cell (CA1 data from Kraus et al., 2013). This legend applies to (C–F). (D) Distribution (top) and cumulative distribution (bottom) of the width of the first firing field for each neuron. (E) Distribution (top) and cumulative distribution (bottom) of the peak rate of each neuron divided by the average rate of each neuron. A smaller value indicates broader firing fields. Vertical black line indicates the maximum difference between cumulative distributions. (F) Distribution of field widths as a function of the time of peak firing. Open circles indicate fields cut off by the end of the treadmill run.

See also Figures S2 and S5 and Table S1.

Wilcoxon rank-sum test: $p = 3 \times 10^{-16}$; Figures 2E and S2F), even as firing fields for both cell types that appeared later during treadmill running were wider (Pearson's linear correlation; grid cells: $\rho = 0.56$, $p = 4 \times 10^{-20}$; non-grid cells: $\rho = 0.65$, $p = 3 \times 10^{-15}$; Figures 2F and S2G). In addition, many grid cells (77; 44%) had two or more firing fields (Figures 1, 2C, 4, and S1; Table S1). In contrast, fewer non-grid cells (27; 18%) had multiple fields (Figure 2C; Table S1) compared to grid cells, $\chi^2(2) = 28.88$, $p = 5 \times 10^{-7}$; and in a previous study (Kraus et al., 2013), we observed only 6% of CA1 cells with multiple firing fields during treadmill running compared to grid cells, $\chi^2(2) = 225.3$, $p \approx 0$. Therefore, parallel to their spatial firing patterns in the open field, the firing patterns of grid cells are characterized by precise, multi-peaked activations while animals run in place. Furthermore, time and distance modulation by grid cells, expansion of field size over time, and multiple firing fields were observed in each animal and brain area studied (see Experimental Procedures), indicating similar temporal coding features among grid cells throughout cortical areas of the hippocampal system.

Spatial Position Cannot Account for Time and Distance Fields

We quantified the degree to which the rat's location systematically varied as a function of the fraction of the treadmill run by determining the area that is visited in each of five evenly divided bins (time bins for time-fixed sessions and distance bins for distance-fixed sessions). We refer to this area as A_{AB} ("AB" stands for "all bins") to distinguish it from the area accounting for 75% of the time spent on the treadmill, which we refer to as A_{75}. The average size of A_{AB} was 44 cm^2 (SD = 24.1 cm^2; minimum [min], 11 cm^2; maximum [max], 156 cm^2), and the rats spent, on average, 80% of the treadmill run within this area (SD = 9%; min, 34%; max, 93%). The average size of A_{75} was 28 cm^2 (SD = 16.3 cm^2; min, 6 cm^2; max, 89 cm^2), and A_{AB} contained, on average, 89% of A_{75} (SD = 12%; min, 30%; max, 100%), indicating that the rats' positions were relatively stable throughout the treadmill run and that each rat spent a majority of the run in the same area.

To quantitatively evaluate the extent to which the observed firing patterns could be explained based on location alone, we used the spatial firing rate map of each neuron (Figure 3) as a look-up table to generate predicted firing rates for that neuron based on the rat's position at each point in the run (time for time-fixed sessions; distance for distance-fixed sessions; see Experimental Procedures). Next, we generated two tuning curves showing the firing rate of that neuron as a function of time or distance spent on the treadmill for both the actual firing (the empirical time or distance tuning curve) and the firing predictions based solely on the spatial firing rate map (the model time/distance tuning curve) (Figure 3). If location is sufficient to explain the observed firing patterns of each neuron, then the two tuning curves for that neuron should match. Alternatively, if the rat was perfectly stationary while on the treadmill, or if the firing of that neuron was completely uncorrelated with location, the model tuning curve should be perfectly flat.

A bootstrap method was used to generate confidence intervals around the time/distance tuning curve for each neuron and to identify regions where the two curves were significantly different. Although nearly all neurons expressed some degree of spatial tuning (indicated by a non-flat model tuning curve), in the majority of neurons with firing fields on the treadmill (155 out of 162 grid cells and 99 out of 113 non-grid cells), there was a region of significant difference between the empirical and model tuning curves, indicating that information about location was not sufficient to explain the firing activity seen on the treadmill. These findings were similar to previous observations

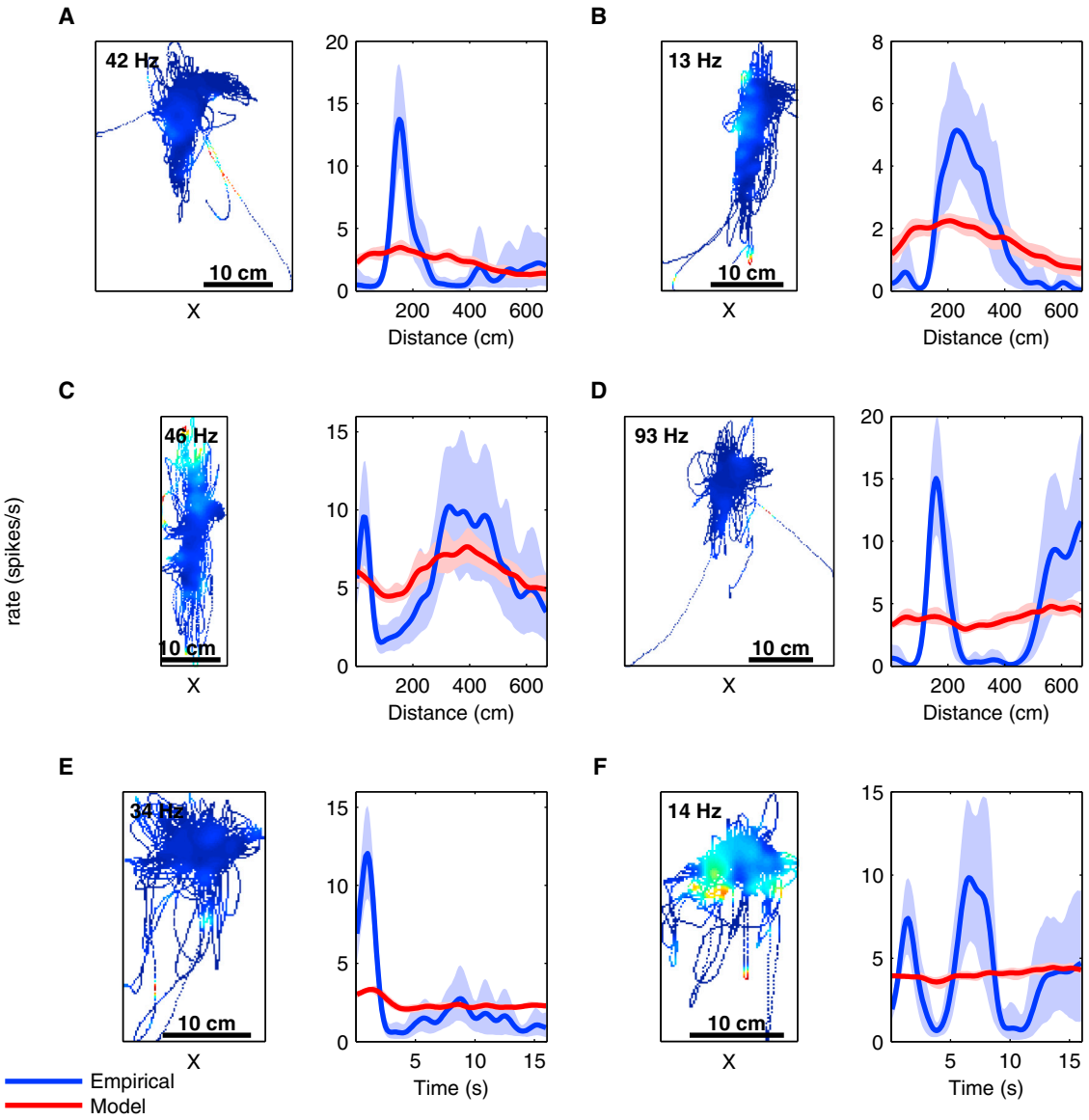

Figure 3. Spatial Activity Cannot Account for Time and Distance Firing Fields

(A–F) Six individual neurons recorded from different recording sessions. For each neuron, there are two panels: the left panel is a spatial firing rate map, and the right panel includes two distance (A–D) or time (E and F) tuning curves. Neurons from distance-fixed sessions (A–D) are plotted in terms of distance run, and neurons from time-fixed sessions (E and F) are plotted in terms of elapsed time. The blue curve is the observed (empirical) tuning curve of a single neuron, calculated based on the actual firing of that neuron. The red curve is the model-predicted tuning curve based on the spatial firing rate map given in the left panel of each pair. Shaded region denotes 95% confidence bounds on firing rates calculated using a bootstrap method. A bin size of 1 pixel × 1 pixel with an SD of 3 pixels was used for this analysis.

of CA1 neurons in animals performing the same task (Kraus et al., 2013), indicating that, during movement in the absence of visual flow, spatial information from visible landmarks and boundaries is not sufficient to drive hippocampal cells or grid cells.

Grid Cells Signal Time Elapsed and Distance Traveled

Punctate activations of grid cells could reflect distance traveled on the treadmill, consistent with the view of grid cells as involved in path integration based on self-generated movement cues (Buzsáki and Moser, 2013; Hafting et al., 2005; McNaughton et al., 2006; Moser et al., 2008), or elapsed time as well as distance during runs, similar to time and distance signals observed in hippocampal neurons (Kraus et al., 2013). Exploiting our design in which treadmill speed varied across laps, we evaluated the extent to which firing could be explained by time and distance separately and found that both factors contribute to differing extents among neurons. Figures 4A and 4B show two examples of grid cells that were more strongly influenced by

distance than time. The firing field in Figure 4B and both firing fields in Figure 4A shifted toward earlier times as the treadmill speed was increased (Figures 4A and 4B, left panels, from top to bottom in the raster plot), but the fields were largely fixed at a particular distance (Figures 4A and 4B, right panels). Conversely, Figures 4C and 4D show two grid cells that were more heavily influenced by time than distance. The field in Figure 4D and the second field in Figure 4C shifted toward farther distances as the speed increased but was fixed at a particular time. Figure 4E shows a non-grid cell that was more heavily influenced by time than distance.

To directly compare the extent to which these dimensions are influential across the populations of grid and non-grid cells, three different generalized linear models (time, distance, and time + distance) were fit to the data to quantify the relative influences of time elapsed and distance traveled. A total of 162 grid cells and 113 non-grid cells were analyzed using this framework (Table S2). 80 grid cells (49%) were significantly influenced by time, $\chi^2(5) > 11.1$, $p < 0.05$; 88 (54%) were significantly influenced by distance, $\chi^2(5) > 11.1$, $p < 0.05$; and 66 grid cells (41%) were significantly influenced by both time and distance during treadmill running (Figures 4F, 4G, S3A, S3B, S3E, and S3F; Table S2). Notably, non-grid cells were also influenced by a combination of time and distance (Figures 4H, 4I, S3C, S3D, S3G, and S3H; Table S2).

We used a pseudo-R^2 measure based on the log-likelihood to determine the degree to which a particular generalized linear model captured the variance in the spike rate for each neuron (see Experimental Procedures). Figure S4 shows the cumulative distribution of the pseudo-R^2 values calculated for each neuron for each of six different generalized linear models. The pseudo-R^2 for the full model (including time, distance, space, spiking history, and treadmill speed) averaged 0.097 (median = 0.089) for grid cells and 0.069 (median = 0.060) for non-grid cells. See Table S3 for average and median pseudo-R^2 values for each generalized linear model and Table S4 for pseudo-R^2 values for the example neurons presented in Figures 1, 4, and S1. This analysis revealed that, on average among grid cells, just time or just distance performed better than just space at capturing the variance in the spike rate and that speed contributed very little. However, for non-grid cells, just space performed better, on average, than just time or just distance. Spiking history was the strongest predictor of spike rate variation, which reflects the nature of neurons in these brain regions to fire in bursts. By including the spiking history in the three generalized linear models that were used in our deviance calculations, we accounted for this potential confound when investigating the impact of time and distance.

During Treadmill Running, the Size and Spacing of Firing Fields for Grid Cells Enlarge Beyond that Expected from Their Properties during Open Field Running

Previous studies have reported that the size and spacing of the spatial fields of grid cells are constant among different familiar environments (Barry et al., 2007, 2012; Fyhn et al., 2007; Hafting et al., 2005). However, in mice traversing a linear track in virtual reality, some grid cells are strikingly aperiodic (Domnisoru et al., 2013), and the scale of grid fields in rats traversing linear tracks differs from that in open fields (Brun et al., 2008; Hafting et al., 2008). Also, proprioceptive and vestibular cues are likely not the same when running in place on a treadmill as when running freely in the open field, and in the treadmill, there is a strong mismatch between self-generated motion cues and the lack of optic flow. Here, we compared the size and spacing of firing fields on the treadmill to those expected from the observed grid cell firing patterns recorded from the same cells when the rats ran in the open field.

A uniform 2D grid field was simulated for each recorded grid cell, using the observed grid cell width and spacing as input to a simulation of the expected grid field pattern in an environment with dimensions as large as the distance traveled on the treadmill. Then, we compared the number, size, and spacing of firing fields observed during treadmill running with both those observed in the open arena and separately with simulated 1D paths through the uniform 2D grid field.

Firing fields observed on the treadmill were much larger and further spaced than those observed in the open field and those predicted by simulations. Also, in nearly every grid cell, many fewer time fields were observed than predicted by these simulations (Figure 5A). In addition, the simulations predicted that when comparing two adjacent fields, the first field should be wider than the second field just as often as the second field is wider than the first field (Figure 5B, inset). In contrast, in nearly all grid cells with two firing fields during treadmill running, the second field was larger than the first field (Figure 5B), paralleling our previous observation of CA1 time cells (Kraus et al., 2013) and suggesting that time and distance representation are non-linear throughout this system. A possible explanation of the differences in number, size, and spacing of fields might be that the grid fields are ''rescaled'' for the distance run, although rescaling observed in extended environments is temporary (Barry et al., 2007). Nonetheless, rescaling predicts a strong correlation between the open field and treadmill field sizes and spacing, but we found no correlation between the simulated and observed first firing field sizes (Figure 5C; $\rho = 0.09$, $p = 0.25$), second firing field sizes (Figure 5C; $\rho = 0.078$, $p = 0.50$), or the spacing (Figure 5D; $\rho = 0.031$, $p = 0.79$). Therefore, the spiking output of grid cells based on purely temporal and self-motion information differs from the spiking output when external cues are available in open arenas and when the dynamics of optic flow during motion registers with temporal and motion cues. Previous simulations demonstrated that both grid cells and time cells could be simulated with the same circuit model (Hasselmo, 2008). Thus, the difference from expected size and number of firing fields found here on the treadmill could be due to the absence of fiducial time signals that could keep the circuit spiking calibrated on the treadmill, in contrast to the presence of fiducial sensory landmarks that keep the grid cell spiking calibrated during movement through space. Time is typically characterized by a scalar coding so that the resolution of timing becomes broader as time advances (Gibbon et al., 1997; Matell and Meck, 2004; Oprisan and Buhusi, 2014). Consistent with scalar coding of time in brain systems, coding of distance by grid cells during movement in the absence of visual calibration involves a systematic enlargement of field size with increasing time elapsed (as is the coding of time in grid cells and CA1 neurons; see Howard and Eichenbaum, 2013).

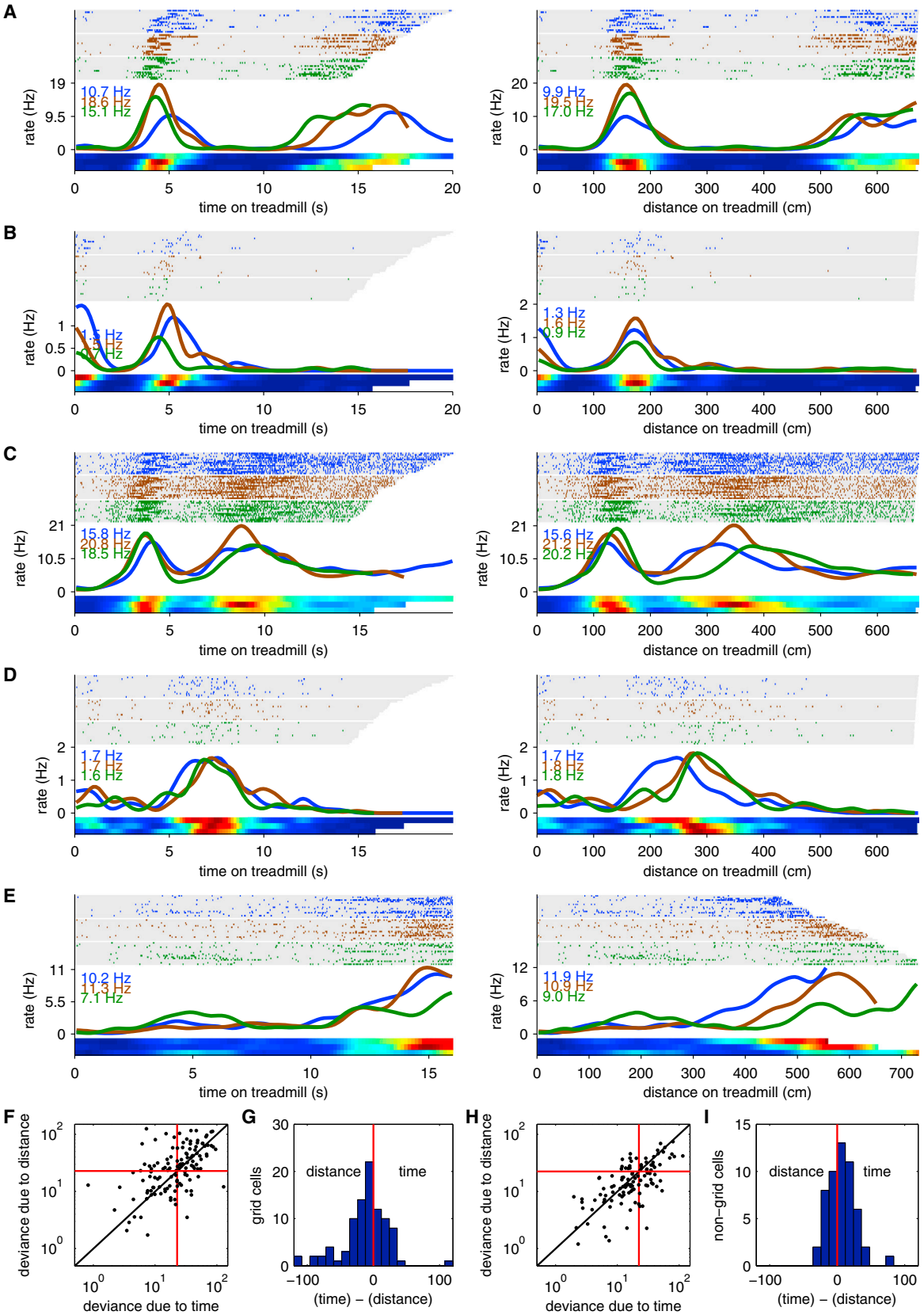

(legend on next page)

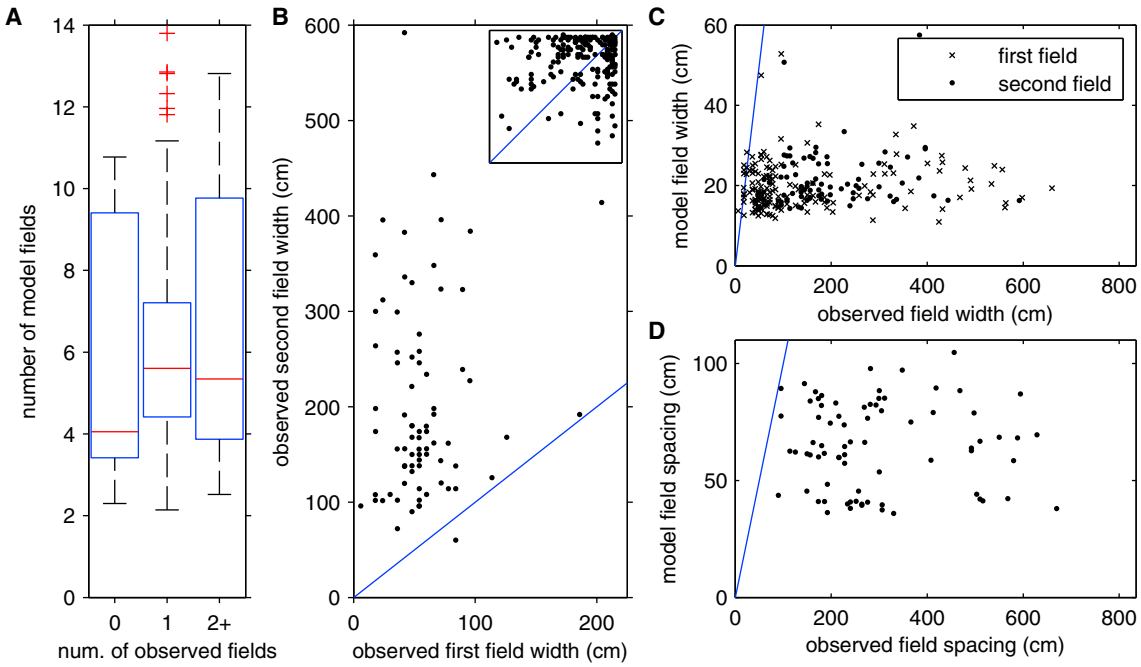

Figure 5. Time Fields on the Treadmill Are Inconsistent with 1D Paths through a 2D Grid Field

(A) Mean number of firing fields observed for each simulation of a grid cell compared to the number of experimentally observed firing fields for that grid cell. Red line indicates median, box extends from the 25% to the 75% percentile, and whiskers extend to full range.

(B) Comparison of the observed first firing field width to the observed second field width in grid cells with multiple fields. (Inset) Comparison of the simulated first field width to the simulated second field width. Contrast simulated results (inset) with observed results in (B).

(C and D) Comparisons of the median simulated first and second field widths (C) and field spacing (D) to the experimentally observed field width and spacing. "First field" includes the only field in neurons where only one field was observed.

DISCUSSION

The present findings inform us about information processing of grid cells during motion in the presence of visual cues but absence of optic flow. These findings bear a superficial similarity to those of Derdikman et al. (2009), who observed a striking fragmentation of grid fields into similar spatial firing patterns as rats ran in one direction repeatedly along each of several parallel alleys of a multi-compartment maze. In this situation, the visual landmarks and optic flow were similar across alleys in each direction, and the findings indicated these cues could drive the spatial firing patterns of grid cells. However, they attributed the fragmentation to visual and tactile segmentation of the environment, rather than constraints on locomotor direction, because the grid field fragmentation was not observed when the rats ran the same repeating movement pattern in an open arena. Here, during one-directional locomotion, when only time and movement cues provide information about distance, a different pattern emerged: grid cell activity signaled a non-linear, often multi-peaked representation of time and distance traveled that is quite distinct from the pattern observed when information about movement from the flow of external cues is available.

Figure 4. Grid Cells Encode Both Distance and Time

(A–E) Examples of treadmill activity of grid cells (A–D) and one non-grid cell (E), whose firing patterns are more consistently explained by distance (A and B) or time (C–E). For each neuron, the same firing activity is plotted as a function of both time since the treadmill started (left panels) and distance traveled on the treadmill (right panels). Blue, brown, and green ticks (and tuning curves) represent the slowest 1/3 of runs, middle 1/3 of runs, and fastest 1/3 of runs, respectively. Numbers in blue, brown, and green indicate the peak firing rate in spikes per second (Hz) of the corresponding group of runs. The rows in the raster plots represent treadmill runs sorted in order of slowest speed (on top) to fastest speed (on bottom).

(F–I) In (F and H), deviance of two GLMs comparing the effect of removing time versus removing distance. The x axis shows the deviance of the space + distance model from the full (space + distance + time) model, effectively measuring the contribution of time to the full model. The y axis shows the deviance of the space + time model from the full (space + distance + time) model, effectively measuring the contribution of distance to the full model. Dots indicate deviances for either grid cells (F) or non-grid cells (H). Dots above the diagonal indicate a stronger influence of distance; dots below the diagonal indicate a stronger influence of time; dots above the horizontal red line are significantly influenced by distance; dots to the right of the vertical red line are significantly influenced by time. Thresholds for significance are based on a chi-square test, taking into account the number of parameters removed from each model (5 degrees of freedom), and adjusted using Bonferroni correction to account for multiple comparisons. (G and I) Strength of time versus distance coding, measured as the difference between time and distance deviances (G) for the grid cells that are shown in (F) and (I) for the non-grid cells that are shown in (H).

See also Figures S3 and S4 and Tables S2, S3, and S4.

Consistent with the path integration view, the firing patterns of grid cells on the treadmill may reflect dead reckoning through computation of path distance from a combination of time traveled (internally generated) and running speed (sensed from treadmill movement or proprioceptive feedback).

Grid cells, along with place cells and other neurons with spatial firing patterns in the hippocampus and interconnected areas, provide the elements of a spatial representation system (Moser et al., 2008). In particular, according to this perspective, grid cells are viewed as central to path integration (McNaughton et al., 2006). Consistent with this view, the present findings provide the first direct evidence of grid cells signaling distance, which is a key element of path integration calculations. However, the same brain system also supports episodic memory, the ability to remember distinct experiences organized in time as well as space (Eichenbaum, 2014), and it has been proposed that the same neural circuitry and algorithms that compute a spatial mapping also support the temporal organization of episodic memories (Buzsáki and Moser, 2013; Hasselmo, 2008, 2012). Here, we extended the evidence supporting a common circuitry, showing that grid cells provide an integrated representation of self-generated time and distance information when location and behavior are held constant. Along with the previous evidence of time and distance coding in the hippocampus (Kraus et al., 2013), the present findings support the view that the hippocampal system organizes representations of experience by a combination of temporal and spatial dimensions in support of memory for episodes in which those dimensions are prominent organizing features.

EXPERIMENTAL PROCEDURES

Subjects and Behavioral and Electrophysiological Procedures

Subjects were four adult male Long-Evans rats, housed individually, kept on food and water restriction, and monitored closely to maintain good health and a minimum of 85% free feeding weight. Animals were given free access to water at the end of the day and on weekends. All animal procedures were approved by the Boston University Institutional Animal Care and Use Committee.

On the first day of training, rats explored a figure-eight maze consisting of a rectangular track (122 cm × 91 cm; 48" × 36") bisected lengthwise by a 122-cm (48")-long central stem (Figure 1A; Movie S1). A 41-cm (16") segment of the center stem was replaced with a commercially available treadmill (Columbus Instruments) adapted to the maze. Two ports for delivering water reward were located in the corners of the maze closest to the start of the central stem, and a third water port was located at the end of the treadmill. The water ports produced an audible click when they were activated.

For clarity, the term "session" is used to refer to an entire training or testing period within a day (typically 40–60 min), the term "trial" is used to refer to one full lap on the maze (starting and ending at either the left or right water port), and the term "run" is used to refer to the period during which the treadmill was moving within a trial (from the moment the treadmill starts to the moment the stop command is sent to the treadmill). The brief period the treadmill took to come to a complete stop was ignored in subsequent analyses. Starting on the second day of training, rats began each session at the start of the central stem. Throughout training, the rats were prevented from turning around. Once a rat progressed forward so their hind legs were on the treadmill, they were given a small water reward at the end of the treadmill and allowed 2 s to drink. The treadmill was then activated at a low speed (5–10 cm/s), and the rat was blocked from running forward off the treadmill while it was moving. The treadmill run was manually aborted, and the treadmill stopped immediately, if the rat either turned around or if its hind legs reached the back edge of the treadmill. The treadmill run was restarted (using the same settings but restarting the elapsed time) once the rat returned to the treadmill facing forward. Aborted runs that occurred during recording sessions were ignored in subsequent analyses. The rat was given another small water reward for running continuously until the treadmill stopped automatically. This reward typically caused the animal to spend the majority of the treadmill run with its mouth positioned close to the water port. The rat was then allowed to either remain on the treadmill or exit the treadmill and finish the lap. If the rat remained on the treadmill, the treadmill was started again, with the same rules as before. When the rat exited the treadmill, it was forced to turn either left or right and was rewarded for reaching the water port in the corner of the maze. Another trial was started when the rat reached the center stem.

During the first few trials, each run lasted only 5–10 s. As the rat grew accustomed to the treadmill, both the treadmill speed and the time required to receive a reward were gradually increased until the rat was consistently running 49 cm/s (maximum speed) for greater than 16 s. At this point, the protocol was changed to either a "distance-fixed" or a "time-fixed" protocol, and the rat was required to complete one trial for each run on the treadmill. In both protocols, the speed on each lap was randomly selected from within a predetermined range. The treadmill speed was held constant throughout each full treadmill run, and a new speed was randomly selected at the start of each treadmill run. In the "distance-fixed" protocol, the duration of each run was adjusted so that the distance traveled was constant (700 cm), regardless of the treadmill speed. In the "time-fixed" protocol, the duration of each run was constant (16 s), regardless of the speed. The minimum speed was chosen based on the lowest speed in which the individual rat ran smoothly on the treadmill. If the treadmill runs too slowly, the rat stops running smoothly and, instead, repeatedly runs forward then rides the treadmill back. The maximum speed was limited by the endurance of the rat and the need to run enough laps to fully sample the range of available speeds. The range of speeds used for recordings was 30 cm/s to 49 cm/s.

Once the rat was comfortable with the randomly varying speeds, it was trained to alternate left and right reward arms until it met a criterion of steady running on the treadmill through the range of speeds used, for at least 40 trials per session, with at least 75% accurate alternation. The total period of training prior to the first recording was between 5 and 25 weeks.

Following training, rats were implanted with microdrives containing 16 independently drivable tetrodes angled ~25° in the posterior direction, which entered the skull through a craniotomy just anterior to the fissure between parietal and postparietal skull bone (approximately anterior-posterior [AP] = −8.0 mm; medial-lateral [ML] = −4.6 mm). Each tetrode consisted of four strands of 0.0005" (12.7-μm) Stablohm 800 wire (California Fine Wire Company), gold plated to reduce impedance to between 180 and 220 kΩ at 1 kHz. At the end of surgery, each tetrode was lowered ~2–3 mm below the dorsal surface. Rats were allowed at least 1 week recovery before training resumed. Tetrodes were slowly advanced toward the MEC.

Electrical recordings were made using two different commercially available systems. The first system was the 96-channel Plexon Multichannel Acquisition Processor (MAP). On this system, each channel was amplified (1,000×–10,000×) and band-pass filtered for high-frequency spiking activity (154 Hz–8.8 kHz). Spike channels were referenced to another electrode to remove movement-related artifacts. Action potentials were detected by threshold crossing and digitized at 40 kHz.

The second recording system was a 64-channel Neuralynx Digital Lynx. Each of the 64 channels (4 channels each, for 16 tetrodes) first passed through a unity-gain VLSI headstage and then into pre-amplifiers. The signals were then amplified (5,000×–20,000×) and band-pass filtered in the 0.3 Hz–6 kHz range and digitized at 32 kHz. Signals were digitally processed online to detect and capture action potentials indicated by threshold crossing on one of the four channels within a tetrode. Custom-built adapters were used to allow the Plexon headstages to interface with the Neuralynx electrode interface board.

To analyze the spatial firing properties of neurons, rats were trained to forage for cut pieces of Kellogg's Froot Loops cereal pieces, distributed randomly throughout an open field environment. Rats were allowed to forage for enough time to visit every region of the environment, typically 10–20 min.

One of two environmental arenas was used for open field foraging. The first environment was located near the Neuralynx recording system and consisted

of a box 162 cm × 115 cm (64" × 45") with walls 30 cm tall. A white cue card was present on one wall of the chamber to provide a stable visual landmark. This environment is hereinafter called the "Neuralynx open field." This environment was used for prescreening and locating grid cells in rats 1, 3, and 4. In addition, for 19 out of 43 sessions for Rat 1 and for 34 out of 43 sessions for rat 3, open field foraging recorded on the Neuralynx open field was paired with treadmill recordings from the Plexon system to classify neurons firing on the treadmill as either grid cell or non-grid cell (see the following section, "Analysis Methods").

The second environment was placed on top of the figure-eight maze (near the Plexon MAP system) and consisted of a black platform (122 cm × 152 cm; 48" × 60") with no walls. This platform is hereinafter called the "Plexon open field." This environment was used for prescreening and locating grid cells in rats 2 and 4 and to conduct open field foraging recordings immediately following treadmill recording sessions for 24 out of 43 sessions for rat 1, for 9 out of 43 sessions for rat 3, and for all sessions for both rats 2 and 4.

Once theta rhythmic neural activity (including grid cells) was detected, treadmill recording sessions were initiated. At this point, tetrodes were turned a maximum of ~32 μm/day, and electrodes were allowed to settle overnight before each recording session. Rats were regularly tested on either the Neuralynx open field (rats 1, 3, and 4) or the Plexon open field (rats 2 and 4) to look for signs of new neural activity. Recordings were made on the treadmill on days that appeared to have neural activity that had not been previously recorded. All treadmill recordings were made using the Plexon MAP system.

For rat 1, all 42 daily recording sessions were distance fixed. For rat 2, all 23 recording sessions were time fixed. For rat 3, the first 34 recording sessions used the time-fixed protocol, and the remaining nine recording sessions were distance fixed. For rat 4, all 27 recording sessions were time fixed. For rat 3, the first few training sessions using the distance-fixed protocol were not used for data analysis.

After recordings were concluded, 40 μA of current was passed through each electrode for 30 s before perfusion and histological confirmation of tetrode placement. Brains were sectioned sagittally at 40 μm and Nissl stained. Histology confirmed that, in both rat 1 (Figure S5A) and rat 2 (Figure S5B), the tetrode tips were located in the MEC. Tetrodes implanted into rat 3 (Figure S5C) were slightly more medial than intended and were not advanced far enough to reach MEC, so those recordings came from the parasubiculum. The microdrive implanted on rat 4 (Figure S5D) was placed more medially, and at a more vertical angle than intended, resulting in recordings in the subiculum and presubiculum. Grid cells have been observed previously in each of these areas (Boccara et al., 2010; Stewart, 2013). To ensure that all neurons analyzed came from regions of the brain that contain grid cells, the non-grid cells used for data analysis came from the same tetrodes and the same recording sessions as grid cells. Figures S5E–S5G show the range of values for gridness, eccentricity, and spacing for grid cells in each of the four rats.

Analysis Methods

For treadmill recordings without accompanying Plexon open field recordings, neurons recorded in the Neuralynx open field were matched to neurons recorded on the same day on the treadmill using primarily the ratios of spike amplitudes between the electrodes in a tetrode. For rat 1, 34 grid cells and 26 non-grid cells were detected using a recording on the Neuralynx open field conducted the same day as the treadmill recording. The remaining 67 grid cells and 41 non-grid cells were recorded on the Plexon open field in the same recording as, and immediately following, the treadmill session. For rat 3, 25 grid cells and 40 non-grid cells were detected using the Neuralynx open field. The remaining 6 grid cells and 13 non-grid cells were detected using the Plexon open field. For both rat 2 and rat 4, all open field recordings were conducted on the Plexon open field immediately following the treadmill session.

Following cluster cutting, all data analysis was performed using custom scripts written for MATLAB (MathWorks). Tuning curves indicating the average firing rate of a single unit as a function of spatial position, time spent on the treadmill, or distance traveled on the treadmill, were calculated by first binning the respective variable and counting the spikes occurring and the amount of time spent in each bin. The spike counts and occupancy times in each bin were independently smoothed by convolving with a Gaussian smoothing kernel, and then the spike counts were divided by the occupancy times to calculate the average firing rate. For spatial tuning curves (also referred to as spatial firing rate maps), we used 3-cm × 3-cm bins and a circularly symmetrical Gaussian kernel with an SD of 3 cm. For temporal tuning curves, we used 150-ms bins and a Gaussian kernel with an SD of 450 ms. For distance (traveled on the treadmill) tuning curves, we used 6-cm bins and a Gaussian kernel with an SD of 18 cm.

In the ensemble time/distance tuning curves, each row represents the tuning curve for a single neuron, normalized by dividing by the peak firing rate of that neuron. For distance-fixed sessions, activity was plotted in units of distance; and for time-fixed sessions, activity was plotted in units of time. Neurons are sorted by the location of peak firing for that neuron.

To quantify a rat's movement through physical space during treadmill running, we divided the space occupied during treadmill running into 1-cm × 1-cm bins and counted the number of video frames the rat spent in each spatial bin. We then ranked the bins in order of decreasing number of video frames and counted the number of bins required to reach 75% of the total video frames spent on the treadmill. This number was then multiplied by the area of each bin (1 cm^2) to get the area that accounted for 75% of the frames spent on the treadmill. We refer to this area as A_{75}: the smaller the value of A_{75}, the less the rat moved through space while on the treadmill.

We also quantified the degree to which the rat's location systematically varied as a function of the time or distance spent on the treadmill. To do this, we took either the distance (for distance-fixed sessions) or the time (for time-fixed sessions) spent on the treadmill and divided it into five evenly divided time/distance bins. We then counted the number of spatial bins that were occupied at least once in each time/distance bin and multiplied that number by 1 cm^2 to get the area that was visited consistently across the entire treadmill run. We refer to this area as A_{AB} ("AB" stands for "all bins") to distinguish it from A_{75}. If the rat's position systematically changed over the time/distance spent on the treadmill, then A_{AB} would be much smaller than A_{75}. However, if the rat's movements were small and uncorrelated with time or distance, then both A_{75} and A_{AB} would be small and would largely overlap.

To test the hypothesis that the observed time and distance modulated firing patterns could be entirely explained by the movement of the rat through space (i.e., place fields), we used the spatial tuning curve for each individual neuron to predict the firing rate of that neuron at each point in time (in time-fixed sessions) or distance (in distance-fixed sessions). This is the same analysis used in Kraus et al. (2013). We started by using the rat's actual spatial position (x and y room coordinates) and spike counts (sampled at 30 Hz) to generate a traditional occupancy normalized spatial tuning curve based on the firing of each neuron, as described earlier (using one camera-pixel-squared bins [approximately 0.2 cm × 0.2 cm] and a SD of 3 pixels). Then, we used the spatial tuning curve as a look-up table: for each video frame, we looked up the rat's actual spatial coordinates in the spatial tuning curve to predict the firing rate of the neuron in that video frame. The result is two vectors for each neuron: one containing the actual spike counts for each video frame and another containing the predicted firing rate based purely on the spatial tuning curve and the rat's trajectory. Then, we divided the time/distance spent on the treadmill into 150-ms (or 6-cm) bins and generated two occupancy-normalized tuning curves for each neuron: (1) an empirical tuning curve that gave the actual average firing rate of the neuron for each bin and (2) a model tuning curve that used the predicted firing rates to calculate the average firing rate for each bin. We then used a bootstrap method to generate confidence intervals around the tuning curve for each neuron. We generated N (N = 1,000) bootstrap samples by randomly sampling (with replacement) the activity of the neuron during a subset of all the treadmill runs during that recording session. For each bootstrap sample, we calculated a tuning curve for both the actual (empirical) firing rates and predicted (model) firing rates for that neuron, and then we calculated the difference between these two tuning curves for each time bin. The result was N empirical tuning curves, N model tuning curves, and N difference curves, which were used to generate 95% confidence bounds on each temporal tuning curve and the difference curve for each neuron (Figure 3). Confidence bounds were adjusted for multiple comparisons by finding group confidence bands using the method detailed in Fujisawa et al. (2008).

We considered significant any time or distance bins in which zero fell outside the confidence bounds of the difference curve, and we considered the

empirical and model curves different if they were significantly different in at least one time bin.

Firing Field Identification

Firing fields during treadmill running were detected by first calculating the mean firing rate (across runs) and the SEM firing rate for each time or distance bin. The mean and SE (multiplied by 1.96) were used to calculate 95% confidence bounds for the firing rate in each bin. Firing fields were defined as adjacent bins where the lower confidence bound exceeded 0 Hz. Each edge of each firing field was determined as the narrower of two conditions: either the lower confidence bound crossed below 0 Hz, or the upper confidence bound crossed below the peak value of the lower confidence bound for that firing field (see sketch in the Figure S2 legend). Multiple firing fields occurred when more than one set of non-adjacent bins met these criterions. Neurons were considered to code time or distance if they had at least one firing field during treadmill running. The space between firing fields was calculated as the distance between the peaks of two adjacent firing fields.

Grid Cell Classification

Each neuron recorded during open field foraging was classified as "grid cell," "non-grid cell," or "uncertain" using a "gridness" algorithm (based on the algorithm used by Sargolini et al., 2006) that was verified independently by three investigators. For each neuron, the spatial tuning curves were calculated using a bin size of 3 cm × 3 cm and a Gaussian smoothing kernel with an SD of 3 cm. An autocorrelation of the spatial tuning curve was then calculated based on Pearson's product-moment correlation coefficient, as described in Sargolini et al. (2006). The six peaks surrounding the center peak of the spatial autocorrelation were then automatically detected, and, if possible, an ellipse was fit to the six peaks. The value of the autocorrelation was sampled at 1° increments around the ellipse to produce a circular vector of 360 samples. A rotational autocorrelation was calculated by rotating the circular vector in increments of 1° and calculating the correlation between the original vector and the rotated vector. The gridness score was computed as the difference between the lowest correlation observed at 60° or 120° of rotation and the highest correlation observed at 30°, 90°, or 150° of rotation.

For each neuron, three different investigators independently visually inspected the spatial firing rate map, spatial autocorrelation, and the trajectory of the rat with spike locations superimposed, and they independently decided whether the neuron was a grid cell or not. During this process, the investigators were able to select which peaks in the autocorrelation were the six peaks that were fit to an ellipse and used by the gridness score calculation. Selecting the peaks was allowed both to correct cases where the automatic peak detection algorithm selected the wrong peaks and to ensure that the grid field spacing was calculated accurately. Neurons were considered "grid cells" only if their gridness scores were positive and if at least two out of three investigators independently agreed that the neuron was, indeed, a grid cell. Neurons were considered "non-grid cells" if their gridness scores were negative and if at least two out of three investigators agreed that they were not grid cells. Otherwise, the neurons were considered "uncertain" and were excluded from further analysis. Only "non-grid cells" that were recorded simultaneously and on the same tetrode as grid cells were used for analysis to ensure that all cells included in the analysis were from brain regions that produce grid cells, the remaining "non-grid cells" were excluded from further analysis. The mean of the distance between the six peaks and the center of the autocorrelation was used as the spacing of the grid field. The semi-major (a) and semi-minor (b) axis of the ellipse connecting the six peaks was used to calculate the eccentricity of each grid cell using the equation $\sqrt{1-(b^2/a^2)}$. The diameter of the center peak of the autocorrelation that exceeded 0.2 was used as the width of the grid fields (Hafting et al., 2005). Figures S5E–S5G show the range of values for gridness, eccentricity, and spacing for grid cells in each of the four rats.

Generalized Linear Model

A generalized linear model (GLM) framework was used to quantify the effects of time, distance, and position on neural activity (Dobson, 2002; Kraus et al., 2013; Lepage et al., 2012; MacDonald et al., 2011; McCullagh and Nelder, 1989; Truccolo et al., 2005). For this analysis, the spiking activity was modeled as an inhomogeneous Poisson process, with the firing rate a function of various covariates that modulate spiking activity (Lepage et al., 2012; MacDonald et al., 2011). During treadmill running, the spiking activity was modeled as:

$$\lambda_{S+T+D}(t) = \lambda_{time}(t) \bullet \lambda_{distance}(t) \bullet \lambda_{space}(t) \bullet \lambda_{speed}(t) \bullet \lambda_{history}(t). \quad (1)$$

Here, $\lambda_{s+t+d}(t)$ is the probability of a spike within each 1-ms time bin ("S," "T," and "D," stand for "space," "time," and "distance," respectively). $\ln(\lambda_{time}(t))$ is a fifth-order polynomial of time relative to the start of each treadmill run (Equation 2); $\ln(\lambda_{distance}(t))$ is a fifth-order polynomial of the distance the belt moved since the start of each treadmill run (Equation 3); $\ln(\lambda_{space}(t))$ is a Gaussian-shaped place field composed of five parameters (Equation 4); $\ln(\lambda_{speed}(t))$ is a first-order polynomial of the treadmill speed (Equation 5); and $\ln(\lambda_{history}(t))$ contains the spiking history of the neuron (Equation 6).

$$\lambda_{time}(t) = e^{\sum_{i=1}^{5} \alpha_i \tau(t)^i}. \quad (2)$$

$$\lambda_{distance}(t) = e^{\sum_{i=1}^{5} \beta_i d(t)^i}. \quad (3)$$

$$\lambda_{space}(t) = e^{\gamma_1 x(t) + \gamma_2 x(t)^2 + \gamma_3 y(t) + \gamma_4 y(t)^2 + \gamma_5 x(t) y(t)}. \quad (4)$$

$$\lambda_{speed}(t) = e^{\delta_1 + \delta_2 s(t)}. \quad (5)$$

$$\lambda_{history}(t) = e^{\sum_{i=1}^{5} \theta_i n(t-(i)ms, t-(i-1)\ ms) + \sum_{i=6}^{11} \theta_i n(t-(25i-120)ms, t-(25i-145)ms)}. \quad (6)$$

In Equation 2, $\tau(t)$ refers to the time since the treadmill last started, and the five α s are parameters that control the degree to which the spike rate is modulated by time. In Equation 3, $d(t)$ refers to the distance the treadmill belt has moved since the start of each treadmill run, and the five β s are parameters that specify the influence of this distance on spike rate. We selected a fifth-order polynomial to model time and distance so we could capture both the sharp onset and offset dynamics of firing fields and multiple peaks in the firing rate. The fifth-order polynomial also uses the same number of parameters (five) as the model for space, allowing for a direct comparison of the deviances between the different models. In Equation 4, $x(t)$ and $y(t)$ refer to the spatial position (x and y room coordinates) of the rat at time t, and five γ s specify the influence of space on spike rate. Spatial position is modeled as a Gaussian-shaped place field and is included in the model to account for any location-specific (i.e., place cell) firing activity. In Equation 5, δ_1 is a constant representing the mean firing rate, $s(t)$ refers to the treadmill speed at time t, and δ_2 specifies the influence of speed on spike rate, consistent with the possibility that speed coding could contribute to path integration (Hartley et al., 2014). In Equation 6, $n(t_1, t_2)$ is the number of spikes that occurred between times t_1 and t_2. The 11 history terms represent five 1-ms bins going back 5 ms (0–1 ms, 1–2 ms, 2–3 ms, 3–4 ms, and 4–5 ms) and six 25-ms bins going back an additional 150 ms (5–30 ms, 30–55 ms, 55–80 ms, 80–105 ms, 105–130 ms, and 130–155 ms). Each history term is modulated by one θ parameter. These time intervals were selected to allow the model to capture the dynamics of both theta and gamma oscillations. Spike history is included in the model to account for the tendency for neurons in this brain region to fire in bursts.

Equation 1 represents the full model encompassing the influence of space, time, and distance on spiking activity (the "S+T+D" model). We similarly defined two nested models:

$$\lambda_{S+T}(t) = \lambda_{time}(t) \bullet \lambda_{space}(t) \bullet \lambda_{speed}(t) \bullet \lambda_{history}(t) \quad (7)$$

and

$$\lambda_{S+D}(t) = \lambda_{distance}(t) \bullet \lambda_{space}(t) \bullet \lambda_{speed}(t) \bullet \lambda_{history}(t). \quad (8)$$

Equation 7 defines the space and time ("S+T") model, and Equation 8 defines the space and distance ("S+D") model.

The parameters for each model (λ_i) were estimated using an iterative Newton-Raphson method to maximize the likelihood function (Γ_i), as described in Lepage et al. (2012). The likelihood function estimates the

likelihood of the firing rate at time t being $\lambda_i(t)$, given the observation of k spikes at time t, assuming a Poisson distribution.

$$\Gamma_i = \prod_t \left(\frac{\lambda_i(t)^{k_t} e^{-k_t}}{k_t!} \right). \quad (9)$$

The resulting maximum likelihoods for each model were then used in likelihood-ratio tests to compare each nested model to the full model to determine whether the additional covariates provided significant information about spiking.

$$D_{(S+T+D)-T} = 2(\ln(\Gamma_{S+T+D}) - \ln(\Gamma_{S+D})). \quad (10)$$

$$D_{(S+T+D)-D} = 2(\ln(\Gamma_{S+T+D}) - \ln(\Gamma_{S+T})). \quad (11)$$

Equations 10 and 11 represent the likelihood-ratio tests used to calculate the deviance of the "S+D" model and "S+T" model, respectively, from the full model due to the removal of the covariates missing from the nested model. The results are shown in Figure 4. Note that $D_{(S+T+D)-T}$ is calculated using Γ_{S+D} (the likelihood of the model with space and distance, but without time) so that the larger the value of $D_{(S+T+D)-T}$, the larger the influence of time on spiking activity above and beyond the influence of the other parameters in the model (such as location-specific firing or spiking history). Under the null hypothesis—that the addition of time to the nested model containing space and distance (as well as speed and spiking history) does not provide more information about spiking activity—the test statistic $D_{(S+T+D)-T}$ has a χ^2 distribution with 5 degrees of freedom. Similarly, under the null hypothesis—that the addition of distance does not provide more information about spiking activity to the nested model already containing space and time—the test statistic $D_{(S+T+D)-D}$ has a χ^2 distribution with 5 degrees of freedom. In performing this analysis, we used Bonferroni correction to correct for multiple comparisons. Next, we subtracted $D_{(S+T+D)-D}$ from $D_{(S+T+D)-T}$ to obtain a measure of the influence of time compared to the influence of distance (Kraus et al., 2013; Lepage et al., 2012; MacDonald et al., 2011) (Figures 4G and 4I).

$$\Delta D_{T-D} = D_{(S+T+D)-T} - D_{(S+T+D)-D}$$

$$\Delta D_{T-D} = 2(\ln(\Gamma_{S+T+D}) - \ln(\Gamma_D)) - 2(\ln(\Gamma_{S+T+D}) - \ln(\Gamma_T))$$

$$\Delta D_{T-D} = 2(\ln(\Gamma_T) - \ln(\Gamma_D)). \quad (12)$$

The value of ΔD_{T-D} will be negative if $D_{(S+T+D)-D} > D_{(S+T+D)-T}$, indicating a stronger influence of distance than time on the spiking activity. Similarly, ΔD_{T-D} will be positive if $D_{(S+T+D)-T} > D_{(S+T+D)-D}$, indicating a stronger influence of time on the spiking activity.

We used a pseudo-R^2 (pR^2) measure based the log-likelihood to determine the degree to which a particular GLM captured the variance in the spike rate.

$$pR^2_M = \frac{\ln(\Gamma_M) - \ln(\Gamma_{Null})}{\ln(\Gamma_{Sat}) - \ln(\Gamma_{Null})}. \quad (13)$$

$\ln(\Gamma_{Sat})$ is the log-likelihood of a saturated model (with one parameter for each instance of time), $\ln(\Gamma_{Null})$ is the log-likelihood of the null model (using just the average spike rate as a predictor), and $\ln(\Gamma_M)$ is the log-likelihood of the model in question. A pseudo-R^2 value of 0 indicates that the model performed no better than the null model, and a value of 1 indicates that the model performed as well as the saturated model. The pseudo-R^2 value was calculated for each neuron for each of six different models. The "Full" model is as described in Equation 1. The remaining five models each used a single set of parameters from the full model, as described in Equations 2–6.

2D Grid Field and 1D Treadmill Path Simulations

A uniform 2D grid field was simulated for each recorded grid cell, using the observed grid cell width and spacing as input to the simulation, and then 1,000 1D paths through the 2D grid field (of the same length as the treadmill run) were simulated. Simulated field widths were defined as the diameter of the fields that exceeded 20% of the peak firing rate. The resulting paths were used to construct a distribution for each grid cell of the expected number of firing fields, field widths, and field spacing. The observed treadmill firing field frequency, width, spacing, and width-to-spacing ratio were then compared to the simulated 1D treadmill paths.

SUPPLEMENTAL INFORMATION

Supplemental Information includes five figures, four tables, and one movie and can be found with this article online at http://dx.doi.org/10.1016/j.neuron.2015.09.031.

AUTHOR CONTRIBUTIONS

Conceptualization and methodology: B.J.K., M.P.B., M.E.H., and H.E.; formal analysis, software, and visualization: B.J.K.; investigation: B.J.K., M.P.B., R.J.R., and M.A.C.; writing of original draft: B.J.K. and H.E.; writing of review and editing preparation: B.J.K., M.P.B., M.E.H., and H.E.; funding acquisition: M.E.H. and H.E.

ACKNOWLEDGMENTS

This work was supported by the following grants: NIMH MH071702, NIMH MH095297, NIMH MH060013, and ONR MURI N00014-10-1-0936.

Received: March 23, 2015
Revised: June 19, 2015
Accepted: September 1, 2015
Published: November 4, 2015

REFERENCES

Barry, C., Hayman, R., Burgess, N., and Jeffery, K.J. (2007). Experience-dependent rescaling of entorhinal grids. Nat. Neurosci. *10*, 682–684.

Barry, C., Ginzberg, L.L., O'Keefe, J., and Burgess, N. (2012). Grid cell firing patterns signal environmental novelty by expansion. Proc. Natl. Acad. Sci. USA *109*, 17687–17692.

Boccara, C.N., Sargolini, F., Thoresen, V.H., Solstad, T., Witter, M.P., Moser, E.I., and Moser, M.-B. (2010). Grid cells in pre- and parasubiculum. Nat. Neurosci. *13*, 987–994.

Bonnevie, T., Dunn, B., Fyhn, M., Hafting, T., Derdikman, D., Kubie, J.L., Roudi, Y., Moser, E.I., and Moser, M.-B. (2013). Grid cells require excitatory drive from the hippocampus. Nat. Neurosci. *16*, 309–317.

Brun, V.H., Solstad, T., Kjelstrup, K.B., Fyhn, M., Witter, M.P., Moser, E.I., and Moser, M.-B. (2008). Progressive increase in grid scale from dorsal to ventral medial entorhinal cortex. Hippocampus *18*, 1200–1212.

Buzsáki, G., and Moser, E.I. (2013). Memory, navigation and theta rhythm in the hippocampal-entorhinal system. Nat. Neurosci. *16*, 130–138.

Davis, B., Christie, J., and Rorden, C. (2009). Temporal order judgments activate temporal parietal junction. J. Neurosci. *29*, 3182–3188.

Derdikman, D., Whitlock, J.R., Tsao, A., Fyhn, M., Hafting, T., Moser, M.-B., and Moser, E.I. (2009). Fragmentation of grid cell maps in a multicompartment environment. Nat. Neurosci. *12*, 1325–1332.

Dobson, A.J. (2002). An Introduction to Generalized Linear Models, Second Edition (Baton Rouge, LA: Chapman and Hall/CRC Press).

Domnisoru, C., Kinkhabwala, A.A., and Tank, D.W. (2013). Membrane potential dynamics of grid cells. Nature *495*, 199–204.

Eichenbaum, H. (2014). Time cells in the hippocampus: a new dimension for mapping memories. Nat. Rev. Neurosci. *15*, 732–744.

Fujisawa, S., Amarasingham, A., Harrison, M.T., and Buzsáki, G. (2008). Behavior-dependent short-term assembly dynamics in the medial prefrontal cortex. Nat. Neurosci. *11*, 823–833.

Fyhn, M., Hafting, T., Treves, A., Moser, M.-B., and Moser, E.I. (2007). Hippocampal remapping and grid realignment in entorhinal cortex. Nature *446*, 190–194.

Gibbon, J., Malapani, C., Dale, C.L., and Gallistel, C. (1997). Toward a neurobiology of temporal cognition: advances and challenges. Curr. Opin. Neurobiol. *7*, 170–184.

Hafting, T., Fyhn, M., Molden, S., Moser, M.-B., and Moser, E.I. (2005). Microstructure of a spatial map in the entorhinal cortex. Nature *436*, 801–806.

Hafting, T., Fyhn, M., Bonnevie, T., Moser, M.-B., and Moser, E.I. (2008). Hippocampus-independent phase precession in entorhinal grid cells. Nature *453*, 1248–1252.

Hartley, T., Lever, C., Burgess, N., and O'Keefe, J. (2014). Space in the brain: how the hippocampal formation supports spatial cognition. Philos. Trans. R. Soc. Lond. B Biol. Sci. *369*, 20120510.

Hasselmo, M.E. (2008). Grid cell mechanisms and function: contributions of entorhinal persistent spiking and phase resetting. Hippocampus *18*, 1213–1229.

Hasselmo, M.E. (2012). How We Remember: Brain Mechanisms of Episodic Memory (Cambridge, MA: The MIT Press).

Howard, M.W., and Eichenbaum, H. (2013). The hippocampus, time, and memory across scales. J. Exp. Psychol. Gen. *142*, 1211–1230.

Huth, J.E. (2013). The Lost Art of Finding Our Way (Cambridge, MA: Belknap Press).

Janssen, P., and Shadlen, M.N. (2005). A representation of the hazard rate of elapsed time in macaque area LIP. Nat. Neurosci. *8*, 234–241.

Kim, J., Ghim, J.-W., Lee, J.H., and Jung, M.W. (2013). Neural correlates of interval timing in rodent prefrontal cortex. J. Neurosci. *33*, 13834–13847.

Kraus, B.J., Robinson, R.J., II, White, J.A., Eichenbaum, H., and Hasselmo, M.E. (2013). Hippocampal "time cells": time versus path integration. Neuron *78*, 1090–1101.

Krupic, J., Bauza, M., Burton, S., Barry, C., and O'Keefe, J. (2015). Grid cell symmetry is shaped by environmental geometry. Nature *518*, 232–235.

Lepage, K.Q., Macdonald, C.J., Eichenbaum, H., and Eden, U.T. (2012). The statistical analysis of partially confounded covariates important to neural spiking. J. Neurosci. Methods *205*, 295–304.

MacDonald, C.J., Lepage, K.Q., Eden, U.T., and Eichenbaum, H. (2011). Hippocampal "time cells" bridge the gap in memory for discontiguous events. Neuron *71*, 737–749.

MacDonald, C.J., Carrow, S., Place, R., and Eichenbaum, H. (2013). Distinct hippocampal time cell sequences represent odor memories in immobilized rats. J. Neurosci. *33*, 14607–14616.

Matell, M.S., and Meck, W.H. (2004). Cortico-striatal circuits and interval timing: coincidence detection of oscillatory processes. Brain Res. Cogn. Brain Res. *21*, 139–170.

Matell, M.S., Meck, W.H., and Nicolelis, M.A.L. (2003a). Interval timing and the encoding of signal duration by ensembles of cortical and striatal neurons. Behav. Neurosci. *117*, 760–773.

Matell, M.S., Meck, W.H., and Lustig, C. (2003b). Not "just" a coincidence: frontal-striatal interactions in working memory and interval timing. Memory *13*, 441–448.

McCullagh, P., and Nelder, J.A. (1989). Generalized Linear Models, Second Edition (Baton Rouge, LA: Chapman and Hall/CRC Press).

McNaughton, B.L., Battaglia, F.P., Jensen, O., Moser, E.I., and Moser, M.-B. (2006). Path integration and the neural basis of the 'cognitive map'. Nat. Rev. Neurosci. *7*, 663–678.

Moser, E.I., Kropff, E., and Moser, M.-B. (2008). Place cells, grid cells, and the brain's spatial representation system. Annu. Rev. Neurosci. *31*, 69–89.

Naya, Y., and Suzuki, W.A. (2011). Integrating what and when across the primate medial temporal lobe. Science *333*, 773–776.

Oprisan, S.A., and Buhusi, C.V. (2014). What is all the noise about in interval timing? Philos. Trans. R. Soc. Lond. B Biol. Sci. *369*, 20120459.

Pastalkova, E., Itskov, V., Amarasingham, A., and Buzsáki, G. (2008). Internally generated cell assembly sequences in the rat hippocampus. Science *321*, 1322–1327.

Poucet, B., Sargolini, F., Song, E.Y., Hangya, B., Fox, S., and Muller, R.U. (2014). Independence of landmark and self-motion-guided navigation: a different role for grid cells. Philos. Trans. R. Soc. Lond. B Biol. Sci. *369*, 20130370.

Roberts, B.M., Hsieh, L.-T., and Ranganath, C. (2013). Oscillatory activity during maintenance of spatial and temporal information in working memory. Neuropsychologia *51*, 349–357.

Sargolini, F., Fyhn, M., Hafting, T., McNaughton, B.L., Witter, M.P., Moser, M.-B., and Moser, E.I. (2006). Conjunctive representation of position, direction, and velocity in entorhinal cortex. Science *312*, 758–762.

Stensola, H., Stensola, T., Solstad, T., Frøland, K., Moser, M.-B., and Moser, E.I. (2012). The entorhinal grid map is discretized. Nature *492*, 72–78.

Stewart, S. (2013). Spatial cells in the subiculum; influence of boundary manipulations. PhD thesis (ProQuest document ID: 1534989864) (United Kingdom: University of Leeds).

Taube, J.S. (1995). Head direction cells recorded in the anterior thalamic nuclei of freely moving rats. J. Neurosci. *15*, 70–86.

Truccolo, W., Eden, U.T., Fellows, M.R., Donoghue, J.P., and Brown, E.N. (2005). A point process framework for relating neural spiking activity to spiking history, neural ensemble, and extrinsic covariate effects. J. Neurophysiol. *93*, 1074–1089.

Watrous, A.J., Tandon, N., Conner, C.R., Pieters, T., and Ekstrom, A.D. (2013). Frequency-specific network connectivity increases underlie accurate spatiotemporal memory retrieval. Nat. Neurosci. *16*, 349–356.